Journal of
Marine Science and Engineering

MDPI

Article

Longitudinal Vibration Transmission Control of Marine Propulsion Shafting with Friction Damper Integrated into the Thrust Bearing

Ganbo Zhang [1,2], Yao Zhao [1,2] and Wei Chu [1,2,*]

1 School of Naval Architecture & Ocean Engineering, Huazhong University of Science & Technology, Wuhan 430074, China
2 Hubei Key Laboratory of Naval Architecture & Ocean Engineering Hydrodynamics (HUST), Wuhan 430074, China
* Correspondence: d201677409@hust.edu.cn; Tel.: +86-027-8754-3258

Abstract: Propeller-induced longitudinal vibration resonance in marine propulsion shafting systems causes great harm to the hull structure and is the primary source of shipboard noise. Integrating a friction damper with designed parameters into thrust bearings can prevent these issues. To investigate the performance of the damper-integrated thrust bearing in longitudinal vibration transmission control, an experimental and theoretical study is carried out in a laboratory-assembled test rig, which consists of components similar to the existing marine propulsion system. We developed a prototype of a thrust bearing designed with a friction-damping generation that allows switching from two supporting states, i.e., damper-connected and damper-disconnected states. Furthermore, a nonlinear analysis method for friction dampers is proposed. By this method, the way in which the friction damper changes the dynamic characteristics of the shafting system is analyzed. Based on the test rig, the acceleration frequency response function (AFRF) of the thrust bearing with and without a friction damper is measured. By comparison, the effectiveness of the friction damper is proved. The experimental results show that the friction damper suppresses the shafting longitudinal vibration response in a broadband frequency range and also confirms the stability of the damping effect, which does not change with the shafting rotational speed or static thrust from the propeller.

Keywords: marine propulsion shafting; longitudinal vibration; friction damper; thrust bearing; test rig; parameter identification; nonlinear system

check for updates

Citation: Zhang, G.; Zhao, Y.; Chu, W. Longitudinal Vibration Transmission Control of Marine Propulsion Shafting with Friction Damper Integrated into the Thrust Bearing. *J. Mar. Sci. Eng.* **2022**, *10*, 1555. https://doi.org/10.3390/jmse10101555

Academic Editors: Carlos Guedes Soares and Serge Sutulo

Received: 21 September 2022
Accepted: 14 October 2022
Published: 20 October 2022

Publisher's Note: MDPI stays neutral with regard to jurisdictional claims in published maps and institutional affiliations.

1. Introduction

For marine vessels, the longitudinal vibration in the shafting system induced by the oscillatory propeller thrust is one of the problems of propulsion. In particular, when the excitation frequency is close or equal to the natural frequency of the shafting system, resonance will occur in the longitudinal direction and cause excessive vibration [1]. It will amplify thrust oscillations transmitted to the hull structure and potentially cause damage.

According to the objects on which the control measures are exerted, there are three methods to reduce the hull longitudinal vibration. The first is to lessen the oscillatory part of the propeller's thrust, focusing on the source of the vibration. The second method is to reduce the response of the hull under exciting forces by improving the structural design, which focuses directly on the hull structure. The last method is to manage the vibration excitation transmitted to the hull by developing or installing control devices on the shafting system, which focuses on the vibration transmission path from the propeller to the hull.

For the first method, certain approaches, such as highly skewed propeller or non-propeller propulsion systems, are used to lower the oscillatory thrust. However, these approaches are difficult to implement due to the complexity of manufacturing and the need to increase technological maturity. For the second method, since the hull structure is mainly designed to meet the requirements of structural strength and general arrangement, there are many limits in terms of structural modification. Furthermore, the vibration response of the hull is not only caused by the propeller; it is hard to achieve an overall vibration-oriented design for the hull structure. Thus, applying control measures to the shafting system to reduce longitudinal hull vibration is more acceptable in practical engineering.

The marine shafting system consists of rotational shafting and irrotational bearings. To prevent longitudinal vibration, there are two control strategies used in practice. One control strategy focuses on rotational shafting and has received much attention. Johnson et al. [2] invented an electromagnetic dynamic vibration absorber (DVA) mounted on the shafting to absorb longitudinal vibration. Baz et al. [3] developed an active pneumatic servo-controller powered by compressed air to impose pressure on the servo-piston coupled to shafting to resist longitudinal vibration. Xie et al. [4] proposed an active multi-strut assembly to attenuate vibration transmission from the shafting to the hull. The other control strategy focuses on the thrust bearing and has also been undertaken by numerous researchers. One of the typical designs proposed by Goodwin [5,6] is the hydraulic resonance changer fitted in a thrust bearing, of which the principle is anti-resonant vibration isolation. Another mechanical resonance changer was invented by William [7], but the principle is traditional vibration isolation. Other devices include magnetic thrust bearing [8,9] and thrust bearing supported by disc springs [10]. Song et al. [11] and Liu et al. [12] conducted theoretical studies on the periodic structure isolator and the anti-resonant isolator for thrust bearing, but did not involve specific devices.

In the literature, it can be observed that more researchers favor the second control strategy; thrust bearing is chosen as the primary carrier to implant the vibration control devices. The possible reasons can be summarized in two ways. On the one hand, the thrust bearing is the nearest component to the excitation source. Vibration control directly applied on thrust bearing can achieve the desired effect without interference from the intermediate parts in the transmission path from propeller to hull. Vibration control devices inserted into the thrust bearing will not interfere with the operation of the shafting system. On the other hand, the thrust bearing is a type of irrotational equipment; adding control devices to the rotational shafting will create more difficulties, for example, in its arrangement and assembly.

Damping is well known to be effective in attenuating vibration, especially in suppressing resonance peaks. However, in previous studies on the control of shafting longitudinal vibration, little attention has been paid to damping technology. One important reason is that there are no effective means to add damping to the shafting system. In this paper, the thrust bearing is also chosen as the carrier of a control device. The proposed passive solution is to introduce Coulomb damping into the thrust bearing. The Coulomb damping is a kind of non-viscous damping, and its principle of suppressing resonance is simple, dissipating vibration energy. In practice, however, there are some technical difficulties in engineering implementation. One problem is how to make a relative motion to generate Coulomb damping in the interior of the thrust bearing. Currently, the marine thrust bearings are the Kingsbury type. The leveling plates support the pivoted tilting pads, as shown in Figure 1, which are a series of upper and lower levers designed to distribute the load evenly between thrust pads. However, the leveling plates belong to the mechanical drive type and cannot damp the longitudinal vibration. To implement Coulomb damping, it is necessary to design a new support structure for thrust pads. The second problem is how to quantify the Coulomb damping to obtain a certain damping effect for shafting, or is greater Coulomb damping better? Furthermore, Coulomb damping is nonlinear; therefore, the following question arises: how can one analyze a shafting system that involves Coulomb damping? This paper examines these problems.

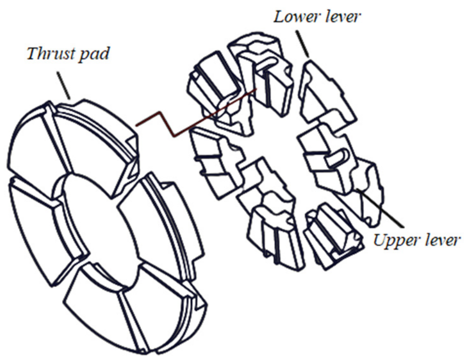

Figure 1. Support structure of the Kingsbury thrust bearing.

The friction damper was developed as a novel support structure for a thrust pad using hydraulic means [13]. It has the integrated advantages of producing Coulomb damping and distributing an uneven load between each pad and is assumed to be a potential alternative to the leveling plates. Coulomb damping has been applied in many engineering fields. In civil and architectural engineering, applications of sliding isolation, which involves inserting a friction surface between the foundation and the base mat of the structure, can be found elsewhere [14]. In automotive engineering, the dry-friction telescopic damper, as a potential substitution for traditional viscous dampers, which may be in suspension, has been developed. Simulation and experimental studies reported that the friction damper exhibited superior performance to the conventional damper [15]. One of the typical characteristics of the Coulomb damping system is discontinuity. When the external force is greater than the maximum static frictional force, the friction pair will slide relatively. Otherwise, the friction pair remains in the sticking state. As a result, the overall behavior of the Coulomb damping system is nonlinear. In view of the nonlinearity of the friction damper and the complexity of the shafting system, the research in this work is based on experiments.

The idea of applying Coulomb damping to control the longitudinal vibration of marine propulsion shafting depends on several key points to be solved in engineering practice. Firstly, a rational and acceptable design to insert the damping generating device into the thrust bearing is needed. Secondly, the level of damping that can be supplied by the damping generating device in practical operation under different conditions should be specified through a sensitive measurement. Finally, the actual effect of the longitudinal vibration control contributed by the Coulomb damping needs to be clarified.

These three key aspects of applying Coulomb damping to control the longitudinal vibration are the main focal points in this paper, which is structured as follows. Firstly, the design for integrating the friction damper into the shafting bearing is introduced, and the operating principle is described. Secondly, the frictional force produced by the friction damper is theoretically analyzed and then measured through experimental means. Thirdly, a test rig assembled to simulate a marine propulsion shafting system is set up and described with a mechanical analysis model, and some uncertain parameters are identified based on an experiment with a particle swarm optimization algorithm. Then, a nonlinear analysis method for a friction damper is proposed, and the way in which the friction damper changes the dynamic behavior of the shafting system is illustrated. Finally, the effectiveness of the friction damper employed to attenuate the transmission of longitudinal vibration in the test rig is experimentally investigated.

2. Design of the Friction Damper Integrated into the Thrust Bearing

Conceptually, the friction damping is produced by a friction surface with normal force pressing against it. As shown in Figure 2, the friction damper integrated into the shaft bearing is assembled with a number of pistons and a support ring. The support ring has a longitudinal tube shape and, around the circumference, is evenly divided into several cylindrical cavities that are interconnected through an annular interior groove to form a connected space. Each piston is assembled inside one cylindrical cavity to reciprocate in the longitudinal direction. To meet the assembling requirements of thrust bearings, the support ring adopts a symmetrical split configuration, in which both the upper and the lower parts are bolted and sealed on the interface. In addition, a radial seal is fitted for each piston for the purpose of sealing all the cavities and then forming an enclosed space; on the other hand, a friction surface is created between the pistons and the support ring. In this way, by filling the connected and enclosed space with oil from the inlet hole, a passive hydraulic system is set up inside the support ring; that is, the pressure of the hydraulic oil balances the propeller's steady thrust. The hydraulic pressure causes internal normal force at the seal outer face against the cavity wall, and consequently, with the tendency of relative motion between the pistons and the support ring, the frictional force is produced.

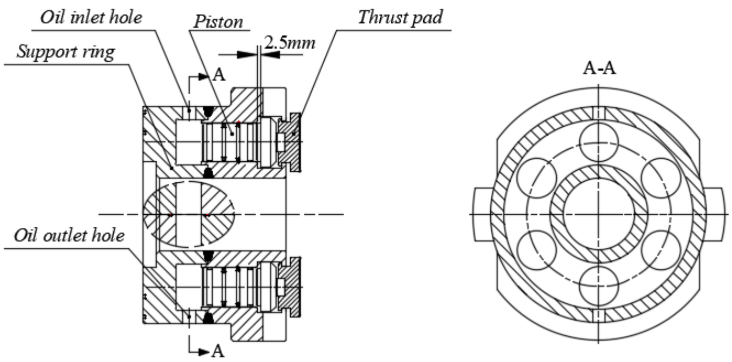

Figure 2. Friction damper integrated into the thrust bearing.

When the propeller rotates and supplies thrust, the steady part of the thrust squeezes oil in the support ring through the pistons, and correspondingly, the oil generates hydraulic pressure. Meanwhile, the oscillation part of the thrust excites the pistons to vibrate relative to the support ring. Under these conditions, the frictional force arises in the friction damper. Apparently, only when the oscillatory thrust exceeds the maximum static frictional force will the relative motion between the pistons and the support ring occur. Therefore, the exciting force transmitted to the thrust bearing is generally less than the maximum static frictional force.

From an experimental point of view, the piston of the friction damper is designed as a convex shape, and more specifically, the diameter of the piston head is larger than that of the piston rod. The piston head is positioned in the middle of the thrust pad and the support ring, with an allowable stroke of 2.5 mm. When there is no hydraulic pressure inside the support ring, for example, the oil outlet hole is open, the piston head is in contact with the support ring under the propeller thrust, and the shafting longitudinal vibration is directly transmitted through the support ring. Thus, the friction damper is short-circuited and does not work. There is, however, hydraulic pressure that balances the propeller thrust, and the piston head is separated from the support ring, while the friction damper is inserted into the shafting longitudinal vibration transmission path to play a damping role. For clarity, the state in which the piston is supported by the support ring is called the 'rigid support state', as shown in Figure 3a, while the state in which the piston is supported by hydraulic oil is called the 'hydraulic support state', as shown in Figure 3b. By switching the support states, the response of the thrust bearing with or without the friction damper can be compared; thus, the effectiveness of the friction damper can be judged.

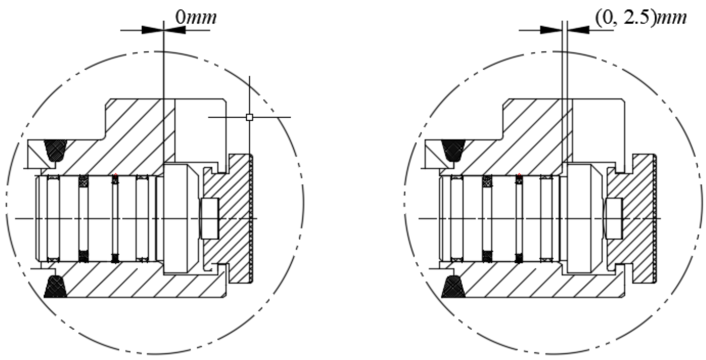

(**a**) (**b**)

Figure 3. The state of friction damping: (**a**) rigid support state; (**b**) hydraulic support state.

3. Analysis and Test of Frictional Force

3.1. Analysis of Frictional Force

According to Coulomb's theory, the frictional force of a friction damper is

$$f = \mu F_n \tag{1}$$

where μ is the coefficient of friction, and F_n is the normal force at the piston seal outer face against the cavity.

The piston friction depends on the seal design. Taking, for instance, the sliding seal, a polytetrafluoroethylene (PTFE)-based ring pre-loaded by an O-ring, the normal force arises from two aspects. One is the contact stress due to the O-ring pre-compression being exerted on the sealing ring; the other is the pressure stress applied by the hydraulic oil being exerted on the sealing ring through the O-ring. The superposition principle is applicable for these two types of compressive stresses [16], so the normal force F_n can be expressed approximately as

$$F_n = \frac{\pi \varepsilon_o E_o + 4\mu_o(1+\mu_o)p}{4(1-\mu_o^2)} s \tag{2}$$

where ε_o, μ_o, E_o denote the O-ring pre-compression, Poisson's ratio, and elastic modulus, respectively; p is the hydraulic pressure; s is the seal outer surface area.

The coefficient of friction μ in Equation (1) is related to the sealing material, surface roughness, lubrication state, relative velocity, and so on, which does not yet have a precise mathematical formulation. Since the coefficient of friction μ is unknown, it is difficult to calculate the frictional force of the friction damper accurately. However, the conclusion can be drawn from Equation (2) that the frictional force has a positive relationship with hydraulic pressure.

3.2. Test and Determination of Frictional Force

In order to determine the actual frictional force, a test device is designed, as shown in Figure 4. The friction damper is connected to a hydraulic circuit composed of an accumulator, valve, pressure transmitter, and hand pump. The oil is pumped slowly to push the piston head to move up to a certain distance from the support ring and then the central retaining nut can be sufficiently hand-tightened. A load plate, which is used to carry a mass block, is placed on one of the pistons. Meanwhile, a dial indicator, which measures the movement, is mounted to contact the load plate. Upon installation, a number of mass blocks are placed on the load plate step by step. Once instantaneous, continuous displacement is observed by the dial indicator and the pressure gauge data and the weight of mass blocks are recorded. The single piston frictional force is equal to the difference in the weight and hydraulic pressure. By changing the initial pressure of hydraulic oil, the frictional force for various pressures can be tested.

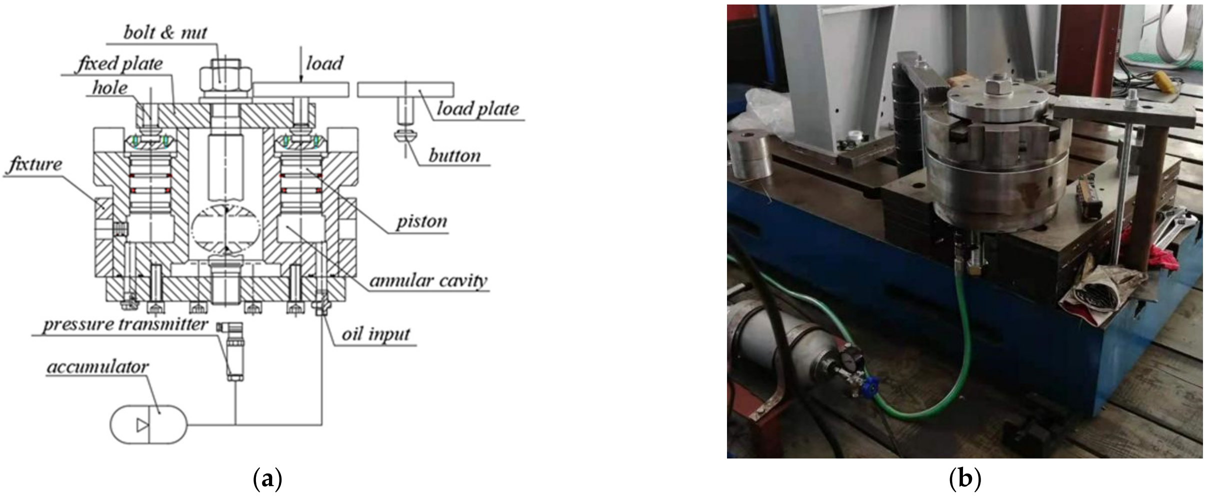

Figure 4. Test device of frictional force: (**a**) schematic diagram; (**b**) photograph.

The tests on two types of piston seals were conducted including the O-ring and the sliding seal ring. Figure 5 provides the tested frictional force. It shows that the frictional forces of the O-ring and sliding seal ring are all positively correlated with the hydraulic pressure, which is consistent with the theoretical conclusion. As the hydraulic pressure increases, the frictional force of the O-ring increases linearly, while the frictional force of the sliding seal ring increases in two stages. When the pressure is below 2 MPa, the frictional force of the sliding seal ring increases sharply. Once the pressure exceeds 2 MPa, the increase in frictional force becomes less steep. With the same hydraulic pressure, the frictional force of the sliding seal ring is much less than that of the O-ring, and with the increase in hydraulic pressure, a greater difference in frictional force between the two types of seals is obtained.

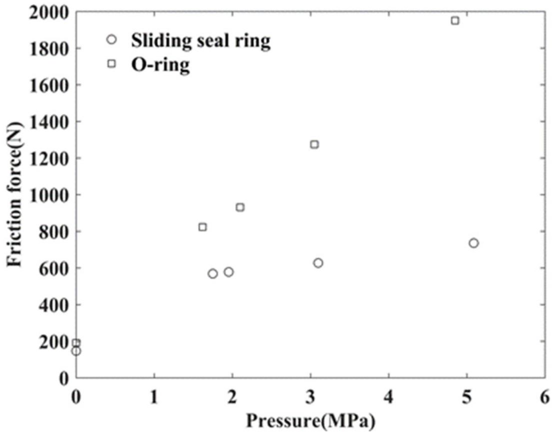

Figure 5. Test results of single piston frictional force with respect to hydraulic pressure.

Essentially, the friction damper dissipates energy under the relative motion of the piston and the support ring. Thus, the maximum static frictional force should not be so large that the relative motion cannot occur. Since the friction coefficient of the material PTFE is much lower than that of the O-ring, the sliding seal is beneficial to improve friction performance and is applied as the seal of the friction damper.

4. Nonlinear Analysis Method of Frictional Force

Because of the existence of frictional force, the friction damper is a nonlinear system. For simplicity, the nonlinear analysis method of the frictional force is explained with a two-degree-of-freedom model, as shown in Figure 6, for which the notations employed are defined as follows. $F(t)$ is the oscillatory thrust, and $f(t)$ is the induced frictional force; both $F(t)$ and $f(t)$ vary over time t. M_p denotes the total mass of forward-thrust pads and pistons, K_h denotes the longitudinal stiffness of oil in a friction damper, and M_t and K_t denote the effective mass and resultant stiffness of the supporting ring, respectively. When the friction damper is integrated into the thrust bearing, M_t and K_t denote the effective mass and resultant stiffness of the thrust bearing block, respectively. The frictional force $f(t)$ has a link with M_p and M_t. In the analysis, the loss factor of the structure has also been taken into account, which is denoted as η_t.

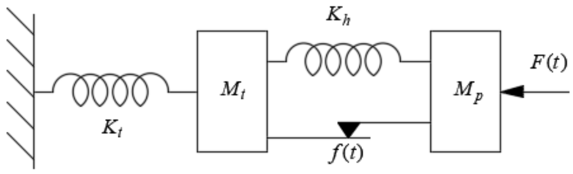

Figure 6. Two-degree-of-freedom model of friction damper.

Referring to Figure 6, with the excitation of oscillatory thrust $F(t)$, the dynamic equilibrium equation of longitudinal vibration can be written as

$$\boldsymbol{M}\ddot{\boldsymbol{x}}(t) + \boldsymbol{C}\dot{\boldsymbol{x}}(t) + \boldsymbol{K}\boldsymbol{x}(t) = \boldsymbol{L}_1 F(t) + \boldsymbol{L}_2 f(t) \tag{3}$$

where the vector $\boldsymbol{x}(\boldsymbol{t}) = \{\boldsymbol{x_p}(\boldsymbol{t}) \quad \boldsymbol{x_t}(\boldsymbol{t})\}^{\boldsymbol{T}}$ denotes the displacement responses in the thrust pads and the supporting ring, and the vectors $\boldsymbol{L_1} = \{\boldsymbol{1} \quad \boldsymbol{0}\}^{\boldsymbol{T}}$ *and* $\boldsymbol{L_2} = \{\boldsymbol{1} \quad -\boldsymbol{1}\}^{\boldsymbol{T}}$ denote the distribution of $\boldsymbol{F}(\boldsymbol{t})$ and $\boldsymbol{f}(\boldsymbol{t})$, respectively; the mass matrix $\boldsymbol{M}$, damping matrix $\boldsymbol{C}$, and stiffness matrix $\boldsymbol{K}$ in Equation (3) are defined as

$$\boldsymbol{M} = \begin{bmatrix} M_p & \\ & M_t \end{bmatrix} \tag{4}$$

$$\boldsymbol{C} = \begin{bmatrix} 0 & \\ & \frac{K_t \eta_t}{\omega} \end{bmatrix} \tag{5}$$

$$\boldsymbol{K} = \begin{bmatrix} K_h & -K_h \\ -K_h & K_h + K_t \end{bmatrix} \tag{6}$$

In Equation (3), the structural damping is transformed into equivalent viscous damping. Moreover, the frictional force $\boldsymbol{f}(\boldsymbol{t})$ is moved to the right-hand side.

The motion of the friction damper consists of two different states, the sticking state and the sliding state. At any instant, the friction damper only belongs to one of the two states. The following conditions that correspond to the two states must be satisfied:

(1) In the sticking state,

$$\begin{cases} \dot{x}_p(t) = \dot{x}_t(t) \\ |f(t)| < f_{max} \end{cases} \tag{7}$$

where $\boldsymbol{f_{max}}$ is the maximum static frictional force.

(2) In the sliding state,

$$\begin{cases} \dot{x}_p(t) \neq \dot{x}_t(t) \\ f(t) = -sgn(\dot{x}_p(t) - \dot{x}_t(t)) f_{max} \end{cases} \tag{8}$$

where $sgn(\ )$ is the sign function. For simplicity, no distinction will be made between the kinetic and the maximum static frictional force.

In the sticking state, the frictional force $\boldsymbol{f}(\boldsymbol{t})$ is less than the maximum static frictional force $\boldsymbol{f_{max}}$ but remains unknown. In the sliding state, however, the frictional force is constant and equal to the maximum frictional force, but with an opposite direction to the relative velocity between the thrust pads and the thrust bearings. Since Equation (3) must hold in the two states, the overall behavior of the friction damper is nonlinear. For a numerical solution, Equation (3) can be further written in the form of state space, as shown below.

$$\dot{\boldsymbol{z}}(t) = \boldsymbol{A}\boldsymbol{z}(t) + \boldsymbol{B}F(t) + \boldsymbol{E}f(t) \tag{9}$$

where $\boldsymbol{z}(\boldsymbol{t}) = \begin{Bmatrix} \dot{x}(t) & x(t) \end{Bmatrix}^T$ is the state vector, and the matrixes $\boldsymbol{A}$, $\boldsymbol{B}$, $\boldsymbol{E}$ in Equation (9) are defined as

$$\boldsymbol{A} = \begin{bmatrix} -\boldsymbol{M}^{-1}\boldsymbol{C} & -\boldsymbol{M}^{-1}\boldsymbol{K} \\ \boldsymbol{I}_{2\times 2} & \boldsymbol{0}_{2\times 2} \end{bmatrix} \tag{10}$$

$$\boldsymbol{B} = \begin{bmatrix} \boldsymbol{M}^{-1}\boldsymbol{L}_1 \\ \boldsymbol{0}_{2\times 1} \end{bmatrix}, \tag{11}$$

$$\boldsymbol{E} = \begin{bmatrix} \boldsymbol{M}^{-1}\boldsymbol{L}_2 \\ \boldsymbol{0}_{2\times 1} \end{bmatrix} \tag{12}$$

The analytical solution of Equation (9) is

$$\boldsymbol{z}(t) = e^{\boldsymbol{A}(t-t_0)}\boldsymbol{z}(t_0) + \int_{t_0}^{t} e^{\boldsymbol{A}(t-\tau)}[\boldsymbol{B}F(\tau) + \boldsymbol{E}f(\tau)]d\tau \tag{13}$$

By employing the discrete time state space formula and assuming that both $F(t)$ and $f(t)$ vary linearly within every time interval, the solution (13) can be written in the following incremental form:

$$z(k+1) = e^{\boldsymbol{A}\Delta t}\boldsymbol{z}(k) + \boldsymbol{B}_0[\boldsymbol{B}F(k) + \boldsymbol{E}f(k)] + \boldsymbol{B}_1[\boldsymbol{B}F(k+1) + \boldsymbol{E}f(k+1)] \tag{14}$$

where k, $k+1$ denote the kth and $(k+1)th$ time step, respectively. The coefficient matrixes are defined as $e^{\boldsymbol{A}\Delta t} = \sum\limits_{i=0}^{\infty} \frac{\Delta t^i}{i!}\boldsymbol{A}^i$, $\boldsymbol{B}_0 = \sum\limits_{i=0}^{\infty} \frac{\Delta t^{i+1}}{i!(i+2)}\boldsymbol{A}^i$, $\boldsymbol{B}_1 = \sum\limits_{i=0}^{\infty} \frac{\Delta t^{i+1}}{(i+1)!}\boldsymbol{A}^i - \sum\limits_{i=0}^{\infty} \frac{\Delta t^{i+1}}{i!(i+2)}\boldsymbol{A}^i$, where Δt is the time interval.

It is noted that on the right-hand side of Equation (14), the frictional force $f(k+1)$ is only unknown at the kth time step. Before the state response $\boldsymbol{z}(k+1)$ is evaluated, $f(k+1)$ must be determined. Unfortunately, the motion of the friction damper has two possible states at any time step. The same problem was encountered in the application of friction pendulum bearings for seismic isolation of the bridge in the reference [17], which presented an important assumption that the isolated bridge was in the sticking state at any instant, initially. Based on the same assumption, the motion of the friction damper at the $(k+1)th$ time step is in the sticking state at first, for which the velocity condition given in Equation (7) must be satisfied as

$$\dot{x}_p(k+1) - \dot{x}_t(k+1) = \boldsymbol{D}\boldsymbol{z}(k+1) = 0 \tag{15}$$

where $\boldsymbol{D} = \begin{bmatrix} 1 & -1 & 0 & 0 \end{bmatrix}$.

By substituting $z(k+1)$ in Equation (14) into Equation (15), the estimated frictional force at the $(k+1)th$ time step is solved as

$$\overline{f}(k+1) = -(D\boldsymbol{B}_1\boldsymbol{E})^{-1}\boldsymbol{D}\Big\{e^{A\Delta t}z(k) + \boldsymbol{B}_0[\boldsymbol{B}F(k) + Ef(k)] + \boldsymbol{B}_1\boldsymbol{B}F(k+1)\Big\} \tag{16}$$

where $\overline{f}(k+1)$ with an overbar emphasizes that the frictional force is an estimated value, obtained by assuming the friction damper to be in the sticking state, which may not be the actual state, and the sign of $\overline{f}(k+1)$ indicates the direction of frictional force produced by the friction damper.

The validity of the above assumption can be verified by the frictional force condition given in Equation (7). If $|\overline{f}(k+1)| < f_{max}$ holds, the friction damper is in the sticking state, and the actual frictional force is

$$f(k+1) = \overline{f}(k+1) \tag{17}$$

Otherwise, if $|\overline{f}(k+1)| \geq f_{max}$, the friction damper is in the sliding state, and the actual frictional force is

$$f(k+1) = sgn\left(\overline{f}(k+1)\right) f_{max} \tag{18}$$

Since the sign of $\overline{f}(k+1)$ indicates the direction of frictional force at the $(k+1)th$ time step, the replacement of the term $-sgn(\dot{x}_p(t) - \dot{x}_t(t))$ in Equation (8) by the term $sgn\left(\overline{f}(k+1)\right)$ in Equation (18) is justified. Once the actual frictional force $f(k+1)$ is determined by Equation (17) or Equation (18), the state response $\boldsymbol{z}(k+1)$ at the $(k+1)th$ time step can be solved by substituting $f(k+1)$ into Equation (14).

For harmonic excitation with amplitude F and circular frequency ω, the response $\boldsymbol{z}(t)$ in the time domain can be computed with the method proposed above. However, the numerical solution is the discrete time state space response $\boldsymbol{z}(k)$ that corresponds to a series of discrete time steps, which is similar to the sample signals of the response in the vibration test. The discrete response $\boldsymbol{z}(k)$ is processed by fast Fourier transform (FFT); then, the response amplitude $\boldsymbol{z}(\omega)$ that corresponds to the excited circular frequency ω can be extracted. It should be noted that the nonlinearity introduced by the frictional force results in the occurrence of subharmonic responses, but these amplitudes are all less than $\boldsymbol{z}(\omega)$. The frequency response is defined as the ratio of $\boldsymbol{z}(\omega)/F$. By sweeping the excited frequency ω in an incremental frequency interval, the acceleration frequency response function (AFRF) of the friction damper can be predicted.

The computational flowchart for the nonlinear analysis method of the frictional force is given in Figure 7.

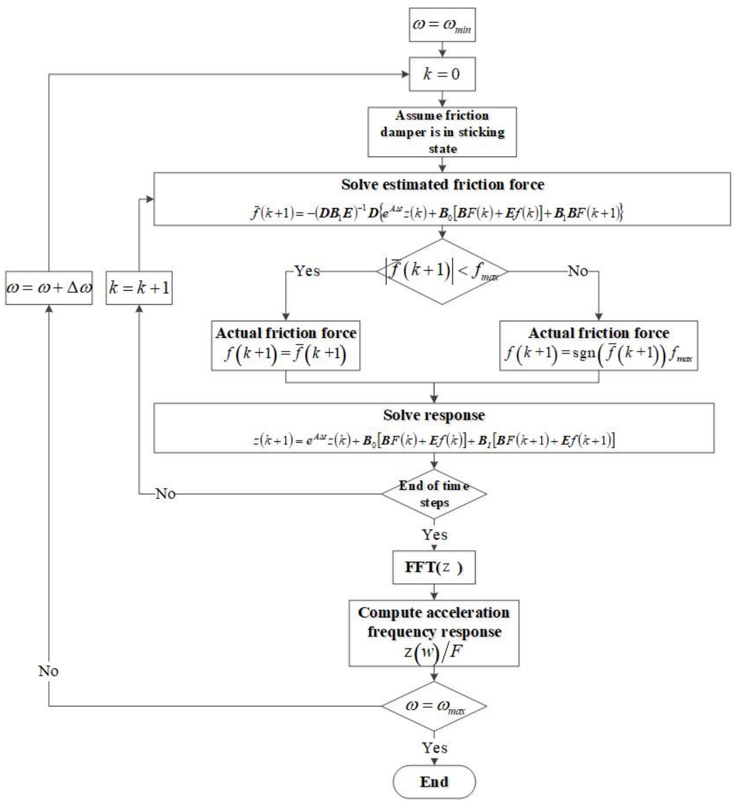

Figure 7. Computational flowchart for the nonlinear analysis method of frictional force.

5. Design and Characterization of Shafting Test Rig

5.1. Design of Shafting Test Rig

A designed test rig with a reduced scale, which is depicted in Figure 8, has been assembled to simulate the marine propulsion shafting system [18] and is taken as the benchmark to assess the effectiveness of the friction damper experimentally. The components of the test rig include a motor, flexible coupling, thrust bearing, stern shafting, intermediate journal bearing, stern journal bearing, weight block, ball spring device, air spring device, excitation rod, bracket, etc. The total length of the shafting is 5 m, and the basic diameter is 105 mm. The thrust bearing integrates the friction damper, and the flexible coupling isolates the motor side from the shafting side. The whole test rig is fixed on the base, which is welded on thick steel plates. In order to further eliminate the disturbance of motor excitation on the thrust bearing, the motor is independently installed on one base, while other test rigs are installed on another base. Furthermore, the electrical control console, hydraulic lubrication system, and air supply system are also configured to meet the use requirements.

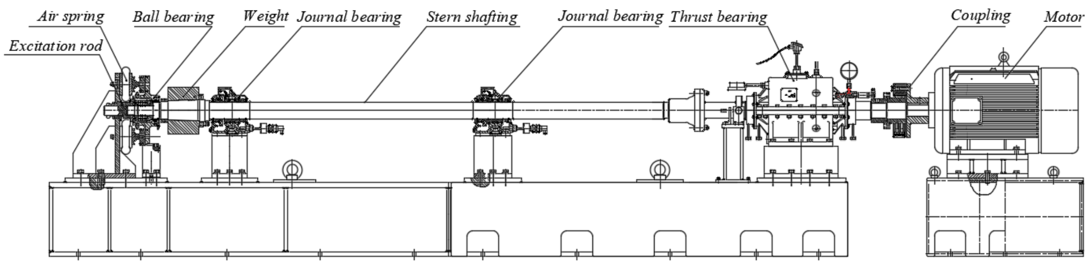

(**a**)

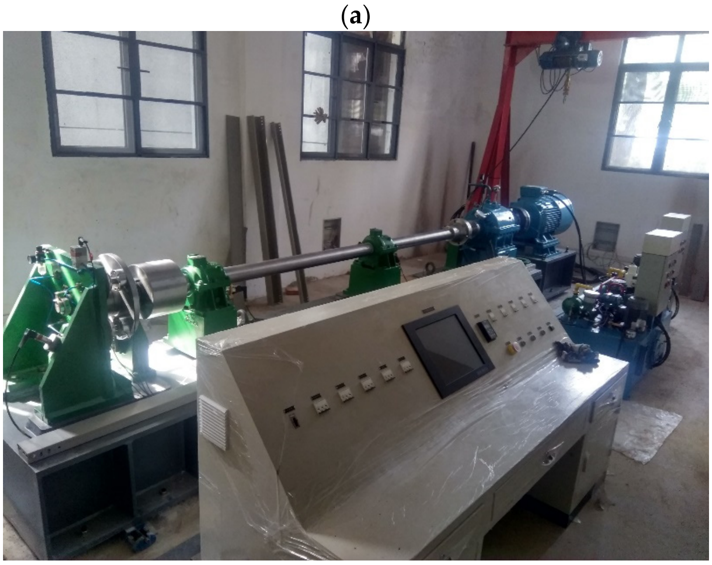

(**b**)

Figure 8. The designed test rig with a reduced scale in the laboratory: (**a**) schematic diagram; (**b**) photograph.

The test rig adopts the method of combining the static load and dynamic excitation at the same time to simulate the propeller propulsion. An air spring device of maximum thrust (55 kN) is fitted in the background of the test rig and is used to apply a static load onto the stern shafting to represent propeller steady thrust. This static load can be easily adjusted by changing the pressure of the air spring. An impact hammer acts as the dynamic source to simulate the excitation of the propeller. The hammer exerts dynamic force in the axial direction on an irrotational excitation rod, which is also fitted at the end of the test rig in combination with the air spring device, to generate shafting longitudinal vibration. For transmitting the static thrust and dynamic force to the shafting simultaneously, a conical ball bearing is sandwiched between the stern shafting and the air spring device. This arrangement is appropriate to solve the problem of connecting the rotational shafting with the irrotational excitation rod.

5.2. Mathematical Model of the Designed Test Rig

The test rig is modeled as a mass-spring damping discrete system, as shown in Figure 9, and the parameters of the components are listed in Table 1. This model covers the range from the air spring device to the flexible coupling and does not contain the friction damper, which is used for analyzing the dynamic characteristics of the shafting system without any control measures applied. While the air spring device imposes static thrust onto the shafting, it also constitutes the elastic boundary and is simplified as a single-degree-of-freedom system.

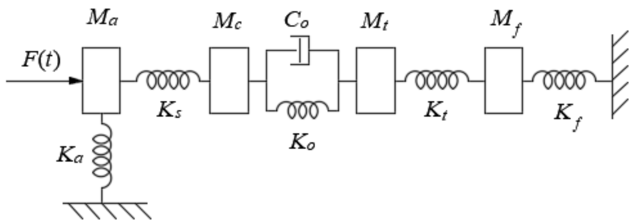

Figure 9. Mathematical model of test rig without control from friction damper.

Table 1. Parameters used in the mathematical model.

Parameter	Symbol	Value
Shafting mass	M_s	360 kg
Shafting stiffness	K_s	5.0×10^8 N/m
Total mass of air spring device and half of shafting	M_a	/
Resultant stiffness of air spring device	K_a	1.0×10^8 N/m
Loss factor of air spring device	η_a	
Total mass of flexible coupling and half of shafting	M_c	200 kg
Damping of lubricating oil film	C_o	/
Stiffness of lubricating oil film	K_o	/
Effective mass of thrust bearing	M_t	/
Resultant stiffness of thrust bearing	K_t	3.4×10^8 N/m
Loss factor of thrust bearing	η_t	/
Effective mass of foundation	M_f	/
Resultant stiffness of foundation	K_f	1.1×10^9 N/m
Loss factor of foundation	η_f	/

The AFRF of thrust bearing is chosen as the dynamic character of shafting longitudinal vibration transmission for analysis. The consideration is that the shafting longitudinal vibration is transmitted to the hull through the thrust bearing. More importantly, the AFRF of the thrust bearing is capable of being measured and calculated so as to ensure the consistency of the assessment index.

The transfer matrix method is used to formulate the AFRF of the thrust bearing. The transfer matrix equation of the test rig is expressed as

$$\begin{Bmatrix} U_f^r \\ F_f^r \end{Bmatrix} = \begin{bmatrix} T_{11}^1 & T_{12}^1 \\ T_{21}^1 & T_{22}^1 \end{bmatrix} \begin{Bmatrix} U_a^l \\ F_a^l \end{Bmatrix} \tag{19}$$

where $\boldsymbol{U}$, $\boldsymbol{F}$ denote the displacement and force, respectively, the superscript $\boldsymbol{l}$, $\boldsymbol{r}$ denote the left end and right end, respectively, the subscript $\boldsymbol{f}$, $\boldsymbol{a}$ denote the thrust bearing base, and air spring device, respectively; $\boldsymbol{T_{11}^1}$, $\boldsymbol{T_{12}^1}$, $\boldsymbol{T_{21}^1}$, $\boldsymbol{T_{22}^1}$ are frequency-dependent complex variables.

According to the rigid boundary condition $\boldsymbol{U_f^r} = \boldsymbol{0}$, the displacement of the air spring device is determined from Equation (19).

$$U_a^l = -\frac{T_{12}^1}{T_{11}^1} F_a^l \tag{20}$$

The transfer matrix equation of the subsystem, ranging from the air spring device to the thrust bearing, is given by

$$\begin{Bmatrix} U_t^r \\ F_t^r \end{Bmatrix} = \begin{bmatrix} T_{11}^2 & T_{12}^2 \\ T_{21}^2 & T_{22}^2 \end{bmatrix} \begin{Bmatrix} U_a^l \\ F_a^l \end{Bmatrix} \tag{21}$$

where $\boldsymbol{T}_{11}^2, \boldsymbol{T}_{12}^2, \boldsymbol{T}_{21}^2, \boldsymbol{T}_{22}^2$ are also frequency-dependent complex variables.

By substituting Equation (20) into Equation (21), the AFRF $\boldsymbol{H}(\boldsymbol{\omega})$ of the thrust bearing yields

$$H(\omega) = \omega^2 \frac{U_t^r}{F_a^l} = \omega^2 \left(-\frac{T_{12}^1}{T_{11}^1} T_{11}^2 + T_{12}^2 \right) \tag{22}$$

5.3. Longitudinal Vibration Experiments and Parameter Identification

The test rig is excited in the axial direction with the impact hammer, and the impact force is superimposed onto a static thrust provided by the air spring device. Two accelerometers are attached to the thrust bearing casing for measuring the acceleration response. Another two accelerometers are diagonally attached to both sides of the thrust bearing seating. It is assumed that the frequency range of interest is between 25 Hz and 300 Hz; thus, the sampling frequency 1280 Hz is used. To minimize the response variation due to random disturbances, test results from five measurements are averaged.

The experiments are conducted in the rigid support state. When the shafting rotational speed is 60 rpm, and the applied static thrust is 30 kN, the measured AFRF of the thrust bearing is as shown in Figure 10. It is observed that the curves of AFRF measured at two points of the thrust bearing casing are almost coincidental, indicating that the casing vibrates globally. A similar situation occurs at the thrust bearing seating. Except for the amplitude, the AFRF measured at the casing and at the seating has the same variation curve. The maximum resonance peak, of which the resonant frequency is 237 Hz, is caused by the global resonance of the test rig, while the other resonance peaks are mainly governed by local resonances.

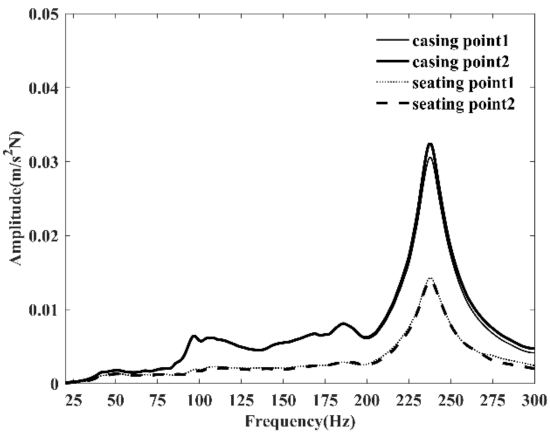

Figure 10. Measured AFRF of thrust bearing without friction damper.

For analyzing the dynamic characteristics of the designed test rig in theory, all the quantifiable parameters must be known. In Table 1, $\boldsymbol{M_s}$, $\boldsymbol{K_s}$ can be computed accurately, and $\boldsymbol{K_a}$, $\boldsymbol{K_t}$, $\boldsymbol{K_f}$ can be obtained based on the results of the thrust-deformation tests. Figure 11 presents the deformations under the action of different thrusts. The thrust is loaded from 5 kN to 55 kN in increments of 5 kN, and the measurements at thrust 5 kN are provided as a reference. It is evident that the stiffnesses are the slope of the fitting lines. $\boldsymbol{M_a}$, $\boldsymbol{M_t}$,

$\boldsymbol{M_f}$ are not equal to the physical mass since the air spring device, thrust bearing, and foundation are assemblies. $\boldsymbol{C_o}$, $\boldsymbol{K_o}$ are difficult to calculate accurately and can only be measured indirectly [19,20]. $\boldsymbol{\eta_a}$, $\boldsymbol{\eta_t}$, $\boldsymbol{\eta_f}$ are uncertain. These parameters need to be identified based on the experimentally measured AFRF of the thrust bearing.

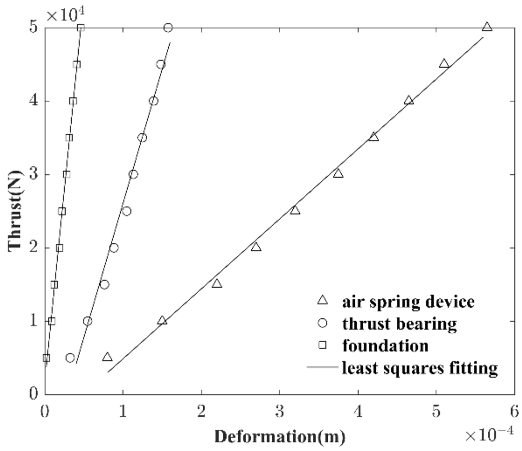

Figure 11. Deformations under the action of different thrusts.

Parameter identification is, in fact, a type of optimization for the identified parameter, and the method used, in general, is residual function optimization. Here, the residual function refers to the difference between the theoretical and experimental AFRF of the thrust bearing. The optimization problem of the shafting parameter identification is described as follows.

(1) Variables: $\boldsymbol{x} = \{\boldsymbol{M_a}, \boldsymbol{\eta_a}, \boldsymbol{K_o}, \boldsymbol{C_o}, \boldsymbol{M_t}, \boldsymbol{\eta_t}, \boldsymbol{M_f}, \boldsymbol{\eta_f}\}$.

(2) Constraints: $\boldsymbol{M_a} \in [\mathbf{0.5},\ \mathbf{2}] \times \mathbf{215.8} + \mathbf{0.5}\boldsymbol{M_s}$, $\boldsymbol{\eta_a} \in [\mathbf{0.01},\ \mathbf{0.35}]$, $\boldsymbol{K_o} \in [\mathbf{0.1},\ \mathbf{10}] \times \mathbf{10^8}$, $\boldsymbol{C_o} \in [\mathbf{0.1},\ \mathbf{10}] \times \mathbf{10^5}$, $\boldsymbol{M_t} \in [\mathbf{0.5},\ \mathbf{2}] \times \mathbf{516.4}$, $\boldsymbol{\eta_t} \in [\mathbf{0.01},\ \mathbf{0.35}]$, $\boldsymbol{M_f} \in [\mathbf{0.5},\ \mathbf{5}] \times \mathbf{386.7}$, $\boldsymbol{\eta_f} \in [\mathbf{0.01},\ \mathbf{0.35}]$.

(3) Objective function: the optimization objective is to minimize the variance in the residual function, which is defined as

$$f(x) = \min \sum_{i=1}^{n} [|H(\omega)| - |H^*(\omega)|]^2 \tag{23}$$

where $H^*(\boldsymbol{\omega})$ is the experimental AFRF of the thrust bearing.

The particle swarm optimization algorithm, which is one of the intelligent evolutionary optimization technologies, is adopted to solve the above optimization problem [21]. Taking the AFRF measured at the thrust bearing casing as a representation of the thrust bearing dynamic characteristic, the parameters are identified as $\boldsymbol{M_a} = \mathbf{332}$ kg, $\boldsymbol{\eta_a} = \mathbf{0.2}$, $\boldsymbol{K_o} = \mathbf{6.3} \times \mathbf{10^8}$ N/m, $\boldsymbol{C_o} = \mathbf{1.1} \times \mathbf{10^4}$ Ns/m, $\boldsymbol{M_t} = \mathbf{284}$ kg, $\boldsymbol{\eta_t} = 0.15$, $\boldsymbol{M_f} = \mathbf{348}$ kg, and $\boldsymbol{\eta_f} = \mathbf{0.1}$. With these identified parameters, the comparison of theoretical and experimental AFRF of the thrust bearing is as shown in Figure 12. It can be observed that the calculated values from the mathematical model coincide with the experimental results very well, and it can be concluded that the model can feasibly simulate the actual longitudinal vibration of the test rig below about 300 Hz.

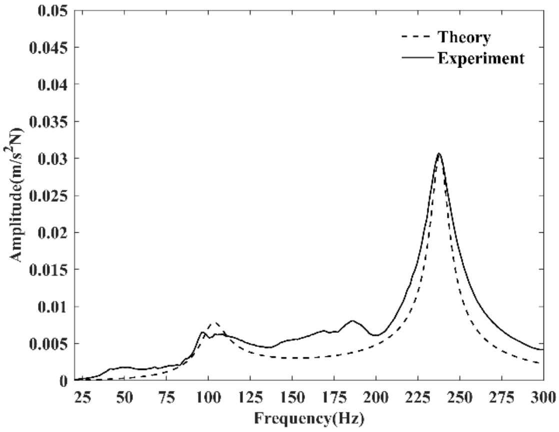

Figure 12. Comparison of theoretical and experimental AFRF of the thrust bearing.

6. Damping Characteristics of Friction Damper

The mathematical model of the test rig with the friction damper is established, as shown in Figure 13.

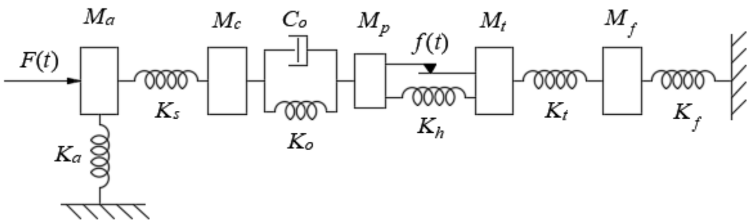

Figure 13. Mathematical model of test rig with friction damper.

In Figure 13, $\boldsymbol{M_p} = \mathbf{24}$ kg, $\boldsymbol{K_h} = \mathbf{1.85} \times \mathbf{10^8}$ N/m, and the other dynamic parameters are all identified. The longitudinal vibration of shafting with a friction damper can be written as Equation (3), where the response vector $\boldsymbol{x}(\boldsymbol{t}) = \left\{ \boldsymbol{x_a}(\boldsymbol{t}) \quad \boldsymbol{x_c}(\boldsymbol{t}) \quad \boldsymbol{x_p}(\boldsymbol{t}) \quad \boldsymbol{x_t}(\boldsymbol{t}) \quad \boldsymbol{x_f}(\boldsymbol{t}) \right\}^{\boldsymbol{T}}$, the distribution vectors of $\boldsymbol{F}(\boldsymbol{t})$ and $\boldsymbol{f}(\boldsymbol{t})$ are $\boldsymbol{L_1} = \left\{ \mathbf{1} \quad \mathbf{0} \quad \mathbf{0} \quad \mathbf{0} \quad \mathbf{0} \right\}^{\boldsymbol{T}}$, $\boldsymbol{L_2} = \left\{ \mathbf{0} \quad \mathbf{0} \quad \mathbf{1} \quad \mathbf{-1} \quad \mathbf{0} \right\}^{\boldsymbol{T}}$, respectively, and the mass matrix $\boldsymbol{M}$, damping matrix $\boldsymbol{C}$, and stiffness matrix $\boldsymbol{K}$ are defined as

$$\boldsymbol{M} = \begin{bmatrix} M_a & & & & \\ & M_c & & & \\ & & M_p & & \\ & & & M_t & \\ & & & & M_f \end{bmatrix} \tag{24}$$

$$\boldsymbol{C} = \begin{bmatrix} \frac{K_a \eta_a}{\omega} & & & & \\ & C_o & -C_o & & \\ & -C_o & C_o & & \\ & & & \frac{K_t \eta_t}{\omega} & -\frac{K_t \eta_t}{\omega} \\ & & & -\frac{K_t \eta_t}{\omega} & \frac{K_t \eta_t}{\omega} + \frac{K_f \eta_f}{\omega} \end{bmatrix} \tag{25}$$

$$\boldsymbol{K} = \begin{bmatrix} K_a + K_s & -K_s & & & \\ -K_s & K_s + K_o & -K_o & & \\ & -K_o & K_o + K_h & -K_h & \\ & & -K_h & K_h + K_t & -K_t \\ & & & -K_t & K_t + K_f \end{bmatrix}. \tag{26}$$

By defining the friction damping ratio as $\xi = f_{max}/F$, the theoretical AFRF of the thrust bearing with a friction damper for various values of ξ is plotted in Figure 14. Compared with the AFRF of the thrust bearing without control, the use of a friction damper can effectively suppress the frequency response, especially at the frequency of the resonance peaks. An increase in resonance peaks with the increase in ξ is observed. It means that the decrease in ξ benefits the damping effect of the friction damper.

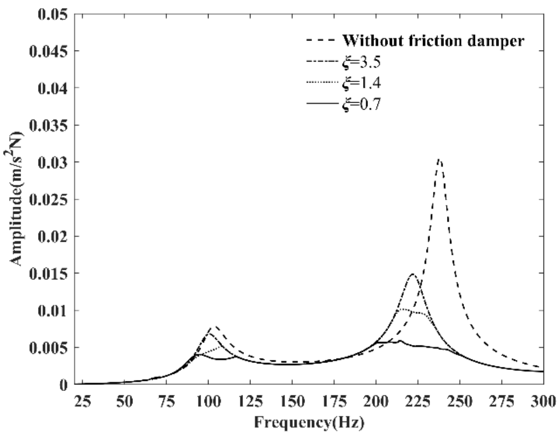

Figure 14. Theoretical AFRF of thrust bearing with friction damper for various values of ξ.

To understand the mechanism of the friction damper used for vibration control, the hysteresis loops of the friction damper for $\xi = 0.7,\ 1.4,\ 3.5$ are further presented in Figure 15. It is worth considering the case when the exciting frequency is 237 Hz, which coincides with the natural frequency of the test rig without control, and the static thrust is 30 kN, which corresponds to the maximum frictional force of 3500 N. The points in Figure 11 denote the correspondence between frictional force and relative displacement at discrete times. The area of the hysteresis loop is equal to the energy dissipated by the friction damper. As ξ increases, the area of the hysteresis loop increases, and the energy dissipation is larger.

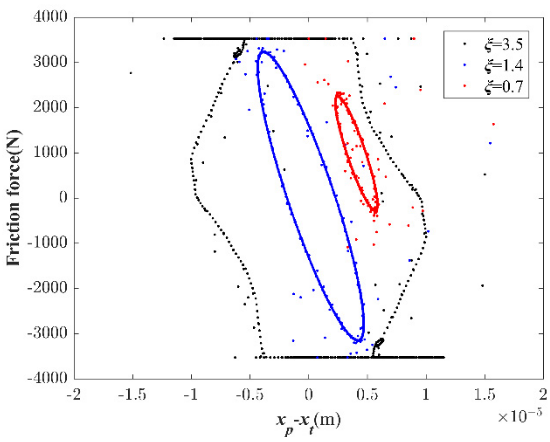

Figure 15. Hysteresis loops of friction damper for $\xi = 0.7,\ 1.4,\ 3.5$.

According to the established friction force nonlinear analysis method, we theoretically predict that the larger the friction damping ratio ξ, the larger the peak FRF, which is not conducive to Coulomb damping. Under the same excitation force, the test results show that the higher the static thrust force, the higher the corresponding peak FRF, which is consistent with the theoretical prediction. Therefore, from the engineering application point, ξ should be designed as small as possible. We suggest that ξ should be less than 1; that is, the maximum static friction should be less than the excitation force amplitude.

This paper uses the particle swarm optimization algorithm to identify the unknown dynamic parameters of the test rig based on the experimental FRF (Section 5.3). Therefore, consistency is the combined result of all the model's dynamic parameters, and each parameter's variations have different influences on FRF. We use the univariate analysis method to change the identification values of the above dynamic parameters one by one, such as increasing them by 10%. The comparison is shown in the Figure 16. It can be observed that, with the accurate identification of the dynamic parameters, changing only one of the dynamic parameter values will not cause a significant deviation between the theoretical FRF and the experimental FRF, which indicates that the established shafting model has good robustness and provides a more accurate model for analyzing the damping effect of friction dampers.

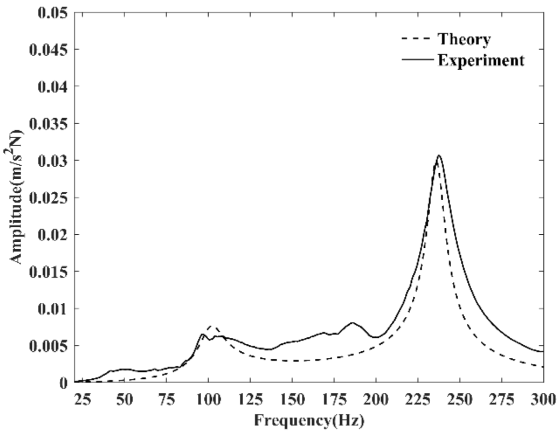

(**a**)

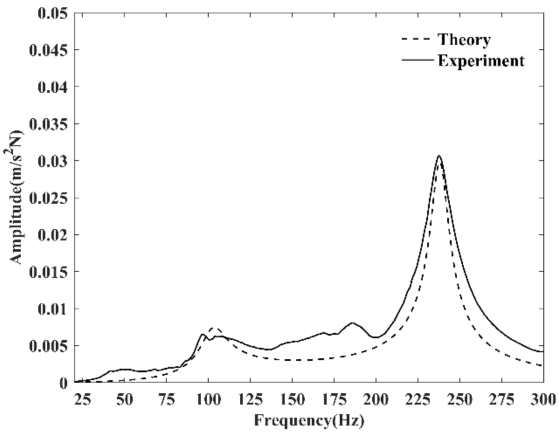

(**b**)

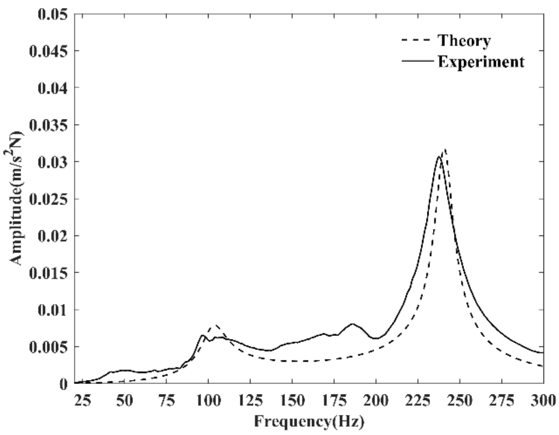

(**c**)

Figure 16. *Cont.*

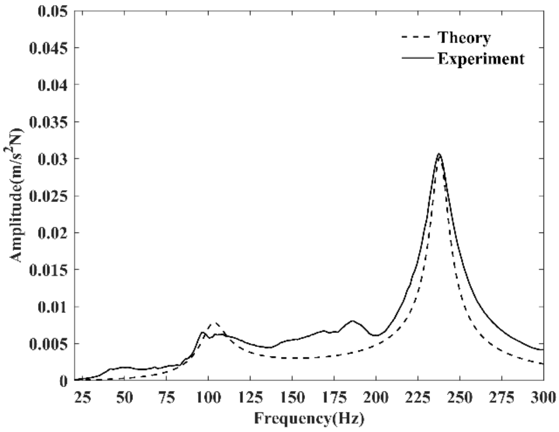

(d)

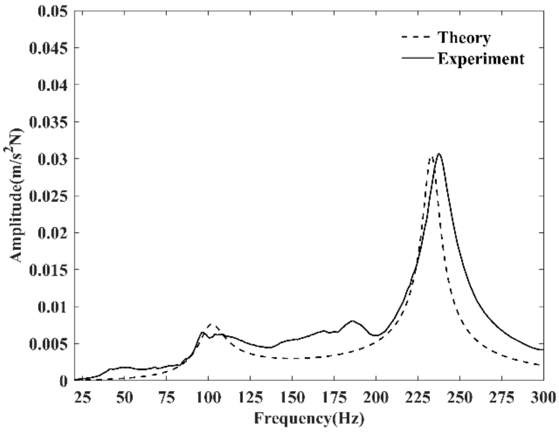

(e)

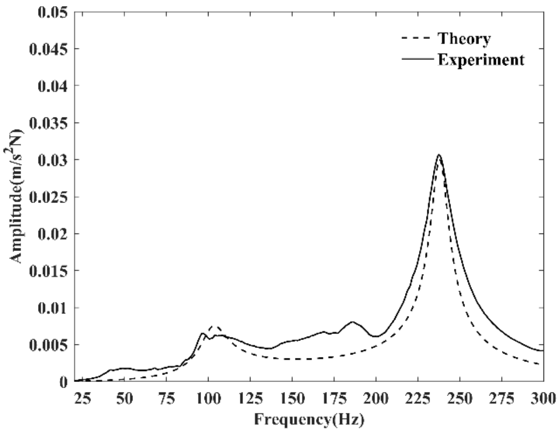

(f)

Figure 16. *Cont*.

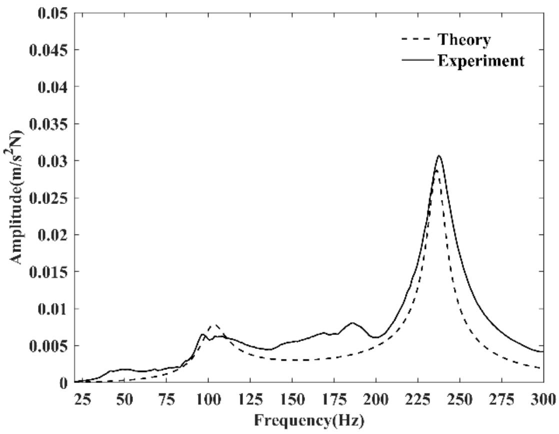

(g)

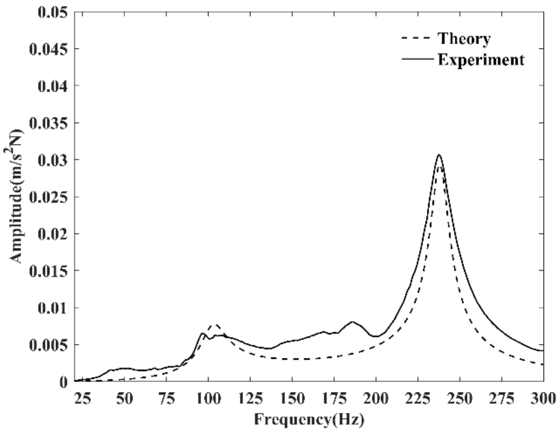

(h)

Figure 16. Effects of different dynamic parameters: (**a**) M_a; (**b**) η_a; (**c**) K_o; (**d**) C_o; (**e**) M_t; (**f**) η_t; (**g**) M_f; (**h**) η_f.

7. Experimental Investigation of Friction Damper

7.1. Damping Effect on Longitudinal Vibration

Following the same test procedure, the AFRF of the thrust bearing with a friction damper was measured. By considering the case that the shafting rotational speed is at 60 rpm and the applied static thrust is 30 kN, the comparison of experimental AFRF of the thrust bearing with and without a friction damper is plotted in Figure 17. It is observed that the response of the thrust bearing is effectively suppressed by the friction damper in a broadband frequency range, which shows the effectiveness of the friction damper in reducing longitudinal vibration transmission in the shafting system. In particular, the attenuation of resonance peaks is very significant, with a maximum reduction of about 75.5%. The straightforward explanation is that the friction damper increases the damping of the thrust bearing, and the friction damping dissipates energy.

Furthermore, the AFRF of the thrust bearing with a friction damper is also predicted by employing the proposed nonlinear analysis method, which is indicated by the dotted line in Figure 17. In the calculation, the value of excitation force $F(t)$ is the same as the sample signals of the hammer impact force in the experiments. As can be observed, the predicted AFRF is close to the measured experimental result in general, except that there is some difference in the maximum resonance peak. This difference may be introduced by other nonlinear factors, such as the assembly clearance that exists in the air spring device and thrust bearing. Generally, the proposed nonlinear analysis method can accurately predict the damping effect of the friction damper and design.

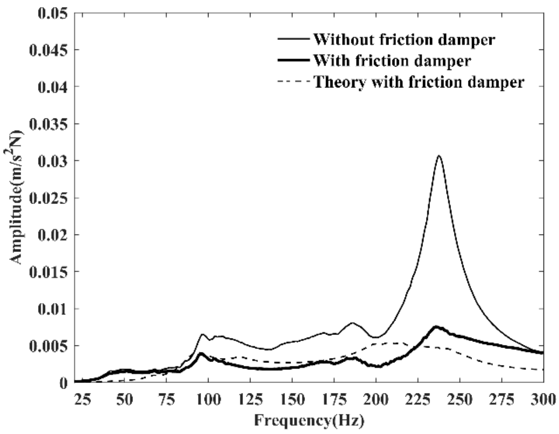

Figure 17. Comparison of experimental AFRF of thrust bearing with and without friction damper.

7.2. Stability of Damping Effect

In order to ensure the stability of the damping effect of the friction damper, a series of tests are carried out for various static thrusts and rotational speeds. The effects of these two variables are studied by means of a single factor test.

Firstly, the influence of rotational speed is investigated in the condition of the same static thrust. The range of rotational speed covers from 60 rpm to 160 rpm, of which the increment 20 rpm is used. Figure 18 shows the comparisons of the AFRF of the thrust bearing with and without a friction damper at different rotational speeds. By comparison, when the static thrust is constant, the resonance peaks of the thrust bearing with a friction damper are always significantly less than those without a friction damper for various rotational speeds. The experimental results indicate that the rotational speed does not affect the damping performance of the friction damper, and the longitudinal vibration characteristics of the shafting system are unrelated to the rotational speed.

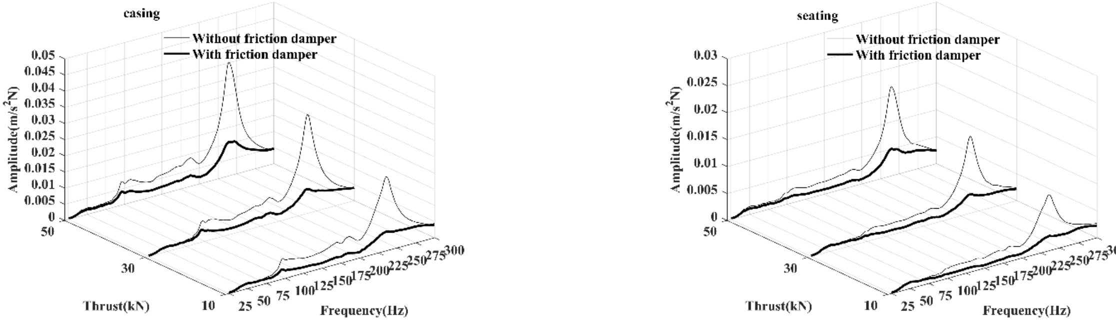

(**a**)

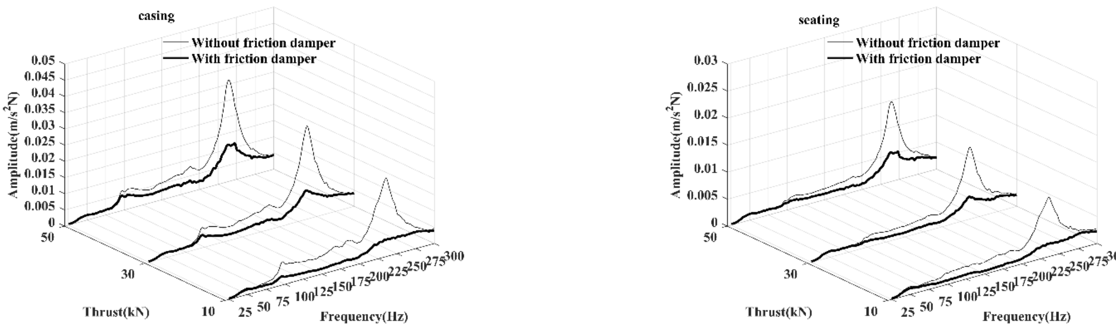

(**b**)

Figure 18. Comparisons of the AFRF of thrust bearing with and without friction damper at different rotational speeds: (**a**) rotational speed at 60 rpm; (**b**) rotational speed at 160 rpm.

The influence of static thrust is investigated under the condition of the same rotational speed. The range of static thrust covers from 10 kN to 50 kN, of which the increment 20 kN is used. Figure 19 presents a comparison of AFRF of the thrust bearing under different static thrusts. Compared with the measurements without control, the AFRFs of thrust bearings with friction dampers under various thrusts are all greatly suppressed in the broadband frequency range, and the attenuation of the maximum resonance peak is particularly significant. It means that the variation in static thrust also has little influence on the performance of the friction damper.

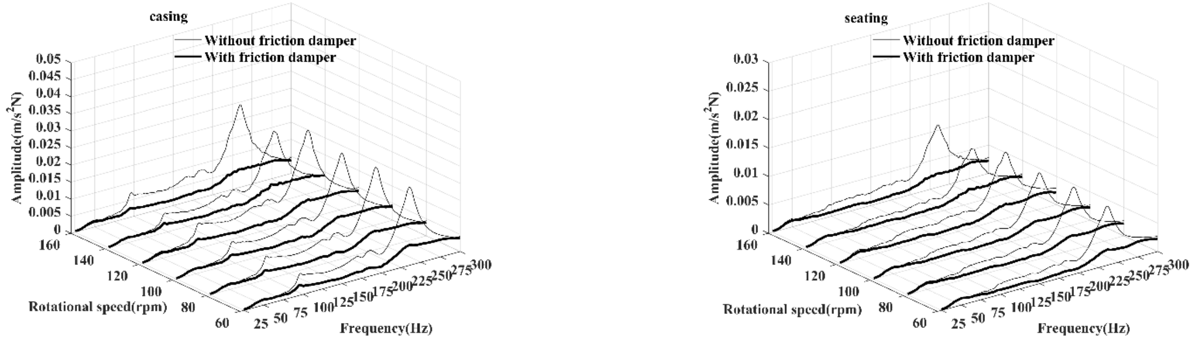

(**a**)

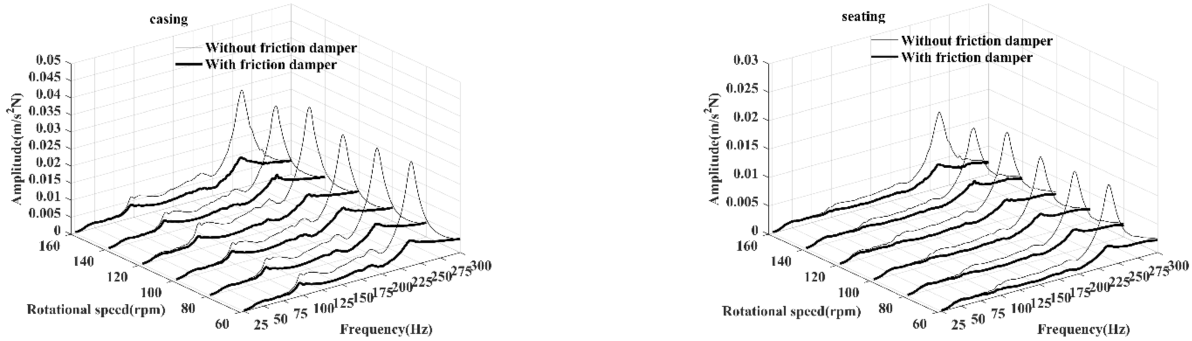

(**b**)

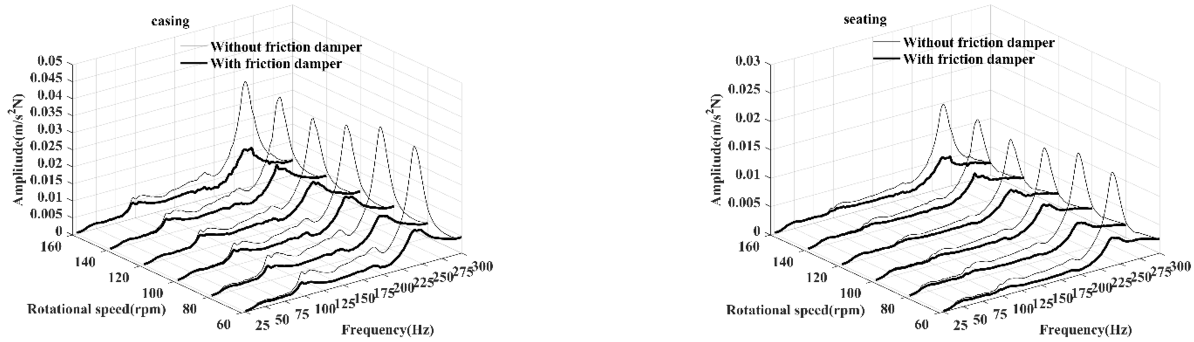

(**c**)

Figure 19. Comparisons of AFRF of thrust bearing under different static thrusts: (**a**) static thrust is 10 kN; (**b**) static thrust is 30 kN; (**c**) static thrust is 50 kN.

One observation is that the resonance peak of AFRF of the thrust bearing with a friction damper increases with the static thrust. Such a variation in resonance is related to the increase in frictional force, which results in an increase in the friction damping ratio. As predicted in theory, the resonance peak increases with the friction damping ratio. The experiments verify the theoretical conclusion.

8. Conclusions

In this work, a friction damper integrated into the thrust bearing was presented to tackle the problem of shafting longitudinal vibration. The choice of using friction damping as a vibration control measure in marine applications is non-conventional; this work conducts an exploratory study in this field.

A test rig was assembled to simulate a marine propulsion shafting system. A prototype of a novel thrust bearing, which provides two operation states for the friction damper device, was also developed. Compared with the traditional thrust bearing, of which the support structure includes upper and lower levers, the invented thrust bearing used hydraulic means. Based on the test rig, the AFRF of the thrust bearing with and without a friction damper was tested. By taking the measurements carried out without control as the benchmark, the effectiveness of the friction damper was assessed. In theory, a nonlinear analysis method for friction dampers was proposed.

The experimental and theoretical results show that the shafting longitudinal vibration response that is normally transmitted through thrust bearings is effectively suppressed by the friction damper in a broadband frequency range. For the test rig, the maximum resonance peak reduction reaches 75.5%, and the damping effect of the friction damper is considerably stable and does not change much with rotational speed and static thrust. The friction damping ratio is the critical parameter that affects the damping effect; a decrease in the friction damping ratio can improve the damping effect. In engineering, the friction damper should be designed according to propeller oscillatory thrust to avoid a redundant piston seal.

Author Contributions: Conceptualization, G.Z. and Y.Z.; methodology, G.Z.; software, G.Z.; validation, W.C., Y.Z.; formal analysis, G.Z.; investigation, G.Z.; resources, Y.Z.; data curation, W.C.; writing—original draft preparation, G.Z.; writing—review and editing, Y.Z.; visualization, W.C.; supervision, Y.Z.; project administration, Y.Z.; funding acquisition, G.Z. All authors have read and agreed to the published version of the manuscript.

Funding: This work was funded by the National Natural Science Foundation of China under Grant No. 51479078 and No. 52101354. Huazhong University of Science and Technology funds the APC.

Institutional Review Board Statement: Not applicable.

Informed Consent Statement: Not applicable.

Data Availability Statement: Not applicable.

Acknowledgments: The authors would like to acknowledge the academic guidance of Chen Xuedong, who helped with the experiments.

Conflicts of Interest: The authors declare no conflict of interest.

References

1. Zhang, G.; Zhao, Y.; Li, T.; Zhu, X. Propeller excitation of longitudinal vibration characteristics of marine propulsion shafting system. *Shock. Vib.* **2014**, *2014*, 1–19. [CrossRef]
2. Johnson, B.G.; Hockney, R.; Eisenhaure, D.; Fenn, R. System and Method for Damping Narrow Band Axial Vibrations of a Rotating Device. U.S. Patent 5291975A, 27 October 1992.
3. Baz, A.; Gilheany, J.; Steimel, P. Active vibration control of propeller shafts. *J. Sound Vib.* **1990**, *3*, 361–372. [CrossRef]
4. Xie, X.L.; Yang, D.Q.; Wu, D. Theoretical analysis on vibration transmission control in a shaft-hull system excited by propeller forces via an active multi-strut assembly. *Ocean. Eng.* **2021**, *221*, 108511. [CrossRef]
5. Goodwin, A.J.H. The design of a resonance changer to overcome excessive axial vibration of propeller shafting. *Trans. Inst. Mar. Eng.* **1960**, *72*, 37–63.
6. Goodwin, A.J.H. Vibration Isolators. U.S. Patent 3202388, 24 August 1965.
7. William, P.W. Thrust Bearing Resonance Changer. U.S. Patent 3937534, 10 February 1976.
8. Lewis, D.W.; Allaire, P.E. Active magnetic control of oscillatory axial shaft vibrations in ship shaft transmission systems part 1: System natural frequencies and Laboratory scale model. *Tribol. Trans.* **1989**, *32*, 170–178. [CrossRef]
9. Lewis, D.W.; Allaire, P.E. Active magnetic control of oscillatory axial shaft vibrations in ship shaft transmission systems part 2: Control Analysis and Response of Experimental System. *Tribol. Trans.* **1989**, *32*, 179–188. [CrossRef]

10. Guo, Q.; Li, Q.; Chen, W.; Yu, Q.; Wang, L.; Li, D. Vibration Reduction of Thrust Bearing with Disc-Spring. Chinese Patent CN102927137A, 13 February 2013.
11. Song, Y.; Wen, J.; Yu, D.; Liu, Y.; Wen, X. Reduction of vibration and noise radiation of an underwater vehicle due to propeller forces using periodically layered isolators. *J. Sound Vib.* **2014**, *333*, 3031–3043. [CrossRef]
12. Liu, N.; Li, C.; Yin, C.; Dong, X.; Hua, H. Application of a dynamic anti-resonant vibration isolator to minimize the vibration transmission in underwater vehicles. *J. Vib. Control.* **2018**, *24*, 3819–3829. [CrossRef]
13. Zhao, Y.; Zhang, G.; Chu, W.; Chang, L. A hydraulic Support Structure of Marine Sliding Thrust Bearing. Chinese Patent CN202011485606.0, 2013.
14. Naeim, F.; Kelly, J.M. *Design of Seismic Isolated Structures: From Theory to Practice*; Wiley: New York, NY, USA, 1999.
15. Guglielmino, E.; Edge, K. A controlled friction damper for vehicle applications. *Control. Eng. Pract.* **2004**, *12*, 431–443. [CrossRef]
16. Müller, H.K.; Nau, B.S. *Fluid Sealing Technology*; Dekker: New York, NY, USA, 1998.
17. Wang, W.; Liu, B.; Zhang, Y.; Shao, X.; Allaire, P.E. Theoretical and experimental study on the static and dynamic characteristics of tilting-pad thrust bearing. *Tribol. Trans.* **2018**, *123*, 26–36. [CrossRef]
18. Zeng, F.M.; Wu, J.M.; Pang, Z.Y. *Principle of Marine Power Plant*; National Defense Industry Press: Beijing, China, 2009.
19. Wang, Y.P.; Chung, L.L.; Liao, W.H. Seismic response analysis of bridges isolated with friction pendulum bearings. *Earthq. Eng. Struct. Dyn.* **1998**, *27*, 1069–1093. [CrossRef]
20. Wang, L.; Fu, Y.; Pei, S.; Xu, H. Theoretical and Experimental Study on the Axial Oil Film Stiffness of Tilting Pad Thrust Bearings. *Tribol. Trans.* **2017**, *60*, 419–427. [CrossRef]
21. Pan, F.; Li, W.X.; Gao, Q. *Particle Swarm Optimizer and Multi-Object Optimization*; Beijing Institute of Technology Press: Beijing, China, 2013.